

Article

Sulphide Globules in a Porcellanite–Buchite Composite Xenolith from Stromboli Volcano (Aeolian Islands, Southern Italy): Products of Open-System Igneous Pyrometamorphism

Alberto Renzulli ¹, Marco Taussi ^{1,*} , Frank J. Brink ², Stefano Del Moro ³ and Richard W. Henley ⁴

¹ Dipartimento di Scienze Pure e Applicate, Università degli Studi di Urbino Carlo Bo, 61029 Urbino, Italy; alberto.renzulli@uniurb.it

² Centre for Advanced Microscopy, The Australian National University, Acton, ACT 0200, Australia; frank.brink@anu.edu.au

³ Geo.In.Tech. srl, Spin Off—Università degli Studi di Urbino Carlo Bo, 61029 Urbino, Italy; stefano.delmoro@geointech.it

⁴ ARC Training Centre for M3D Innovation, Research School of Physics, The Australian National University, Acton, ACT 0200, Australia; richard.henley@anu.edu.au

* Correspondence: marco.taussi@uniurb.it



Citation: Renzulli, A.; Taussi, M.; Brink, F.J.; Del Moro, S.; Henley, R.W. Sulphide Globules in a Porcellanite–Buchite Composite Xenolith from Stromboli Volcano (Aeolian Islands, Southern Italy): Products of Open-System Igneous Pyrometamorphism. *Minerals* **2021**, *11*, 639. <https://doi.org/10.3390/min11060639>

Academic Editor: Monica Piochi

Received: 6 May 2021

Accepted: 15 June 2021

Published: 16 June 2021

Publisher's Note: MDPI stays neutral with regard to jurisdictional claims in published maps and institutional affiliations.



Copyright: © 2021 by the authors. Licensee MDPI, Basel, Switzerland. This article is an open access article distributed under the terms and conditions of the Creative Commons Attribution (CC BY) license (<https://creativecommons.org/licenses/by/4.0/>).

Abstract: Pyrometamorphism is the highest temperature end-member of the sanidinite facies (high-temperature, low-pressure contact metamorphism) and comprises both subsolidus and partial melting reactions which may locally lead to cryptocrystalline-glassy rocks (i.e., porcellanites and buchites). A wide range of pyrometamorphic ejecta, with different protoliths from Stromboli volcano, have been investigated over the last two decades. Among these, a heterogeneous (composite) glassy sample (B1) containing intimately mingled porcellanite and buchite lithotypes was selected to be studied through new FESEM–EDX and QEMSCAN™ mineral mapping investigations, coupled with the already available bulk rock composition data. This xenolith was chosen because of the unique and intriguing presence of abundant Cu–Fe sulphide globules within the buchite glass in contrast with the well-known general absence of sulphides in Stromboli basalts or their subvolcanic counterparts (dolerites) due to the oxygen fugacity of $\text{NNO} + 0.5\text{--NNO} + 1$ (or slightly lower) during magma crystallization. The investigated sample was ejected during the Stromboli paroxysm of 5 April 2003 when low porphyritic (LP) and high porphyritic (HP) basalts were erupted together. Both types of magmas are present as coatings of the porcellanite–buchite sample and were responsible for the last syn-eruptive xenoliths' rim made of a thin crystalline-glassy selvage. The complex petrogenetic history of the B1 pyrometamorphic xenolith is tentatively explained in the framework of the shallow subvolcanic processes and vent system dynamics occurred shortly before (January–March 2003) the 5 April 2003 paroxysm. A multistep petrogenesis is proposed to account for the unique occurrence of sulphide globules in this composite pyrometamorphic xenolith. The initial stage is the pyrometamorphism of an already hydrothermally leached extrusive/subvolcanic vent system wall rock within the shallow volcano edifice. Successively, fragments of this wall rock were subject to further heating by continuous gas flux and interaction with Stromboli HP basalt at temperatures above 1000 °C to partially melt the xenolith. This is an open system process involving continuous exchange of volatile components between the gas flux and the evolving silicate melt. It is suggested that the reaction of plagioclase and ferromagnesian phenocrysts with SO_2 and HCl from the volcanic gas during diffusion into the melt led to the formation of molecular CaCl in the melt, which then was released to the general gas flux. Sulphide formation is the consequence of the reaction of HCl dissolved into the melt from the gas phase, resulting in the release of H_2 into the melt and lowering of f_{O_2} driving reduction of the dissolved SO_2 .

Keywords: igneous pyrometamorphism; gas–solid reactions; buchite; porcellanite; hydrothermally-altered volcanics; sulphide; pyrrhotite; Stromboli; Aeolian Islands

1. Introduction

Pyrometamorphism is a type of thermal metamorphism involving very high temperatures—often to the point of melting in suitable lithologies at low pressures—that has been extensively reviewed by Grapes [1]. Pyrometamorphic rocks are micro-cryptocrystalline to glassy, as the result of processes of recrystallization and melting/crystallization under high temperature/low pressure conditions. The term *pyrometamorphism* (from the Greek *pyr/pyro*: fire; *meta*: change; *morph*: shape or form) was first used by Brauns [2] to describe high temperature changes taking place at the immediate contact of magma and country rocks with or without metasomatic processes. The high temperatures can be provided by magma (i.e., igneous pyrometamorphism), spontaneous combustion of coal, carbonaceous sediments, oil and gas (giving rise to the so called paralavas), or lightning that strikes at the surface. All of these conditions characterize the sanidinite facies of metamorphism (Figure 1).

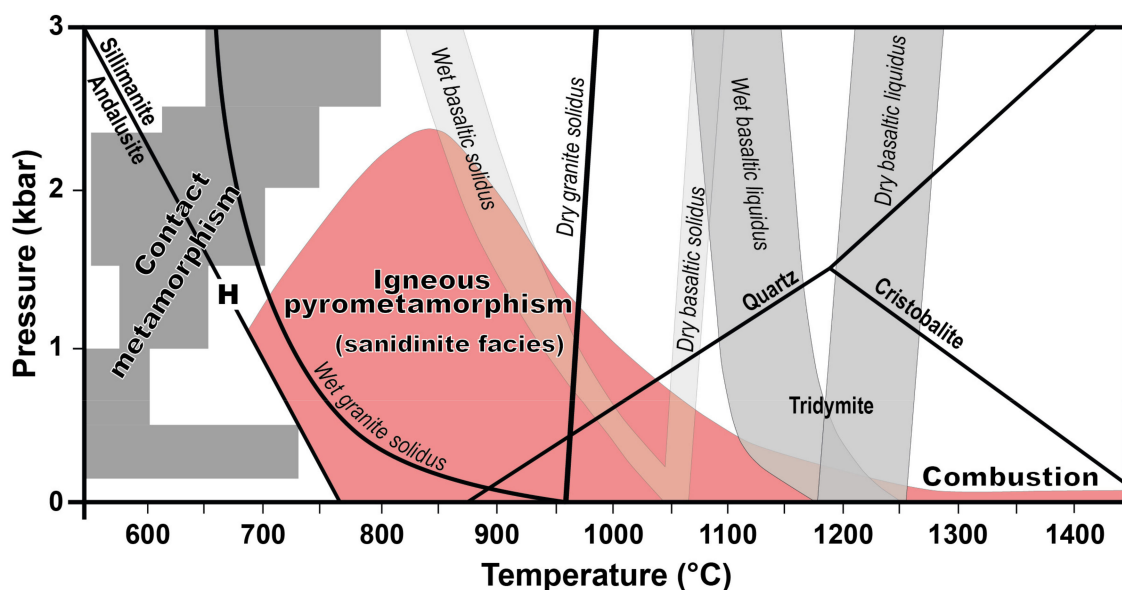


Figure 1. The Petrogenetic Grid at low pressure ($P < 3$ kbar) showing a relationship of igneous pyrometamorphism (sanidinite facies rocks) with lower temperature contact metamorphism (modified from [1]). P–T estimates of contact aureole rocks are from Barton et al. [3], wet/dry basalt solidus of various basalt compositions after Yoder and Tilley [4], wet/dry granite solidus from Tuttle and Bowen [5], andalusite/sillimanite transition (H) from Holdaway [6], quartz/tridymite/cristobalite inversion curves from Kennedy et al. [7] and Ostrovsky [8].

Following the nomenclature descriptions and definitions given by Grapes [1], the products of igneous pyrometamorphism principally comprise two rock types:

1. *Buchite*. A partly to almost completely vitrified rock resulting from intense contact metamorphism. The term was coined by Mohl [9]—probably after the German geologist Leopold Von Buch [10]—to describe fused rocks in contact with basalt, replacing the term *basalt jasper*. Although then applied to partially melted sandstones [11], buchite was later used to describe fused pelitic rocks [12].
2. *Porcellanite*. A light colored, very fine grained, completely recrystallized pyrometamorphosed clay, marl, or shale—originally named from a naturally baked clay considered to be a variety of jasper [13] which led to the adoption of the now obsolete term *porcelain-jasper*.

The additional term “emery” is used by Grapes [1] to describe dark, hard, and dense granular rock consisting mainly of corundum, spinel, magnetite, and/or ilmenite–hematite, formed by high (near basaltic magma) temperature metamorphism of laterite or aluminous (pelitic) sediments.

Non-modal melting and rapid mineral reaction rates driven by extreme temperature gradients that vary by several hundred degrees over a few metres or centimetres [1] lead to the formation of numerous high temperature minerals, many of which are only found in pyrometamorphic rocks.

Igneous pyrometamorphic rocks are most commonly exposed in contact aureoles of mafic intrusions where mechanical erosion of wall rocks of suitable composition may lead to concentrations of xenoliths in sills and dykes, such as observed in thin (up to 6 m wide) mafic sills and dikes of the Ross of Mull Peninsula, Scotland [14,15], or along the contact of a steeply dipping pipe-like body such as Blaue Kuppe, Germany [16]. By contrast, they rarely can be seen in active volcanoes, mainly because they occur as xenoliths that have been entrapped by the erupting magma shortly after the occurrence of very high-T, low-P pyrometamorphic reactions.

Among the igneous pyrometamorphic xenoliths that have been found as ejecta from active volcanoes, Grapes [1] notes the Stromboli samples studied by Salvioli-Mariani et al. [17] and interpreted as derived from the crustal basement (metapelites) below the volcano. By contrast, igneous pyrometamorphic xenoliths affected by vapour-phase crystallization are reported at Vesuvius, Italy (indialite-bearing; [18]) and Mt. Ruapehu volcano in New Zealand (osumilite- and indialite-bearing; [19]). Grapes [1] also emphasized that the protoliths of the pyrometamorphic xenoliths found in White Island volcano, New Zealand [19,20] are acid-sulphate hydrothermally-altered vent andesitic breccia and tuff. Indeed, hydrothermally-altered rocks may strongly resemble pelites in terms of their bulk rock chemistry and therefore are potential lithologies that might be transformed into igneous pyrometamorphic rocks. This is the case for most of the Stromboli buchite ejecta studied by Del Moro et al. [21] that often contain relicts of porphyritic textures. Del Moro et al. [21] argue that the likely source rock for these buchite ejecta was a member of the Upper Vancori volcanic sequence underlying the Neostromboli and Recent Stromboli edifice that had undergone extensive leaching before being pyrometamorphosed by the present-day basalt along the magma conduit walls. The leaching is due to the persistent activity of Stromboli volcano with eruptions of pyroclastic material (basaltic scoriae, lapilli and ash) that normally accumulate within the crater area (also called “crater terrace”, where several active vents are always present) and are continuously subject to burial, reheating and intense chemical alteration due to the incessant degassing of the underlying magma system. A suite of anhydrite-bearing lapilli tuff ejecta from Stromboli studied by Del Moro et al. [22] may be interpreted as related to heterogeneous gas (SO₂) reactions with Ca-bearing minerals in low pressure solfataric alteration environment deposits (in and below the crater terrace), at temperatures from 600 to above 800 °C, as suggested by Fegley and Prinn [23], Ayris et al. [24], Henley et al. [25], and Henley and Seward [26]. As recently demonstrated by Henley and Fischer [27], sub-surface mineral-gas reactions between common calcic minerals and SO₂ to produce anhydrite and reduced sulphur exert a profound control on the redox state and total sulphur concentration of high temperature volcanic gases.

Among the igneous pyrometamorphic ejecta of Stromboli already described by Del Moro et al. [21], this research focuses on the composite xenolith B1 (erupted during the 5 April 2003 paroxysm) which is a mixture of white porcellanite and dark buchite (Figure 2). Both the volatile-rich, low porphyritic (LP) basaltic magma (generally involved in the paroxysms of Stromboli) and the high porphyritic (HP) basalt (i.e., the magma characterizing the persistent activity and commonly stored in the uppermost part of the subvolcanic system) are found as a mantle of the investigated pyrometamorphic xenolith B1. We report new micro-analytical data (FESEM-EDX and QEMSCANTM) in conjunction with bulk rock analyses of this sample from Del Moro et al. [21]. Glass of the buchite portion of B1 is uniquely crowded with microspheres of Fe-Cu sulphides (hereafter globules) otherwise not present in modern (and past) Stromboli eruptive products because of the oxygen fugacity of the present-day Stromboli magma (at least for the low porphyritic basalts as described in Section 2) being between $\text{NNO} + 0.5$ and $\text{NNO} + 1$ [28–31]. Understanding of the formation

of these recently discovered immiscible sulphide globules requires development of a more complex multistage petrogenetic history of the porcellanite–buchite xenolith, with respect to the simple two-stage interpretation (i.e., closed system igneous pyrometamorphism on hydrothermally altered volcanics of the edifice cone) previously proposed by Del Moro et al. [21] for the shallow buchite suite ejecta of Stromboli. To form the multiphase quenched sulphide globules (S^{-2}), a relative change in the redox state of S is necessary during the evolution of the buchite ejecta and therefore an open system igneous pyrometamorphism is needed, emphasizing the role played, besides magma, by high temperature gas–solid reactions (between SO_2 –HCl gas and calcium silicate phase). Sulphide globules were also recognized (but not analysed) by Salvioli-Mariani et al. [17] in another vesicle-rich buchite ejecta sample from Stromboli (sample PST 107), and the presence of sulphides in lithotypes resulting from pyrometamorphism is common [1].

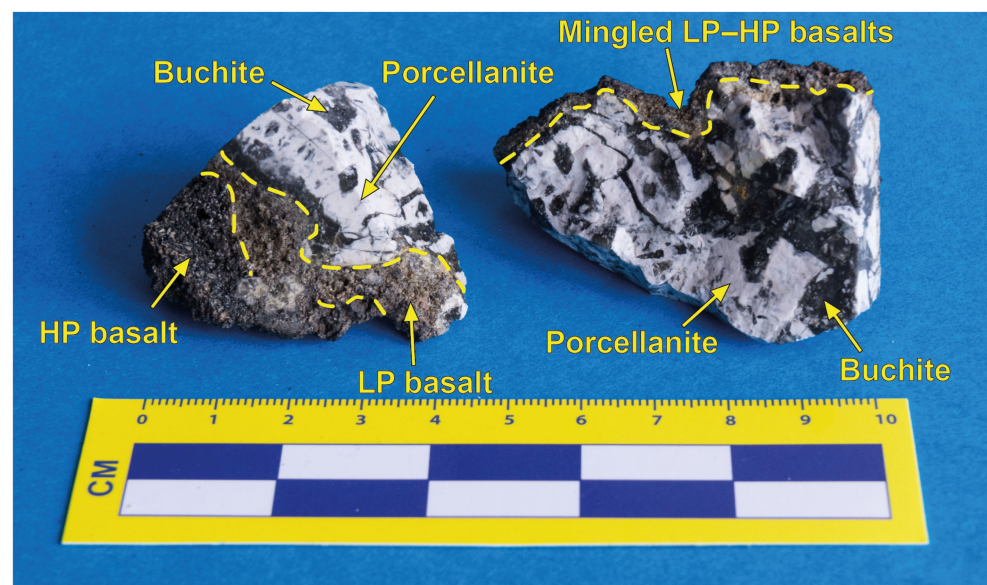


Figure 2. Two fragments of the composite B1 xenolith consisting of white porcellanite and dark buchite. Cuscate–convolute contacts between porcellanite and buchite portions are highlighted, as well as the juvenile basalt coating the sample. Both HP (highly porphyritic, black scoria) and LP (low porphyritic, highly vesicular “golden” pumice) are emphasized, as distinct magmas or mingled with each other. It is worth noting that the LP basalt is only involved during the paroxysmal eruption of Stromboli such as that of the 5 April 2003 when the porcellanite–buchite xenolith erupted.

2. Geology and Magmatism of Stromboli Volcano

Stromboli is a stratovolcano of the Aeolian Islands (Tyrrhenian Sea, Italy; Figure 3) that rises 924 m a.s.l. and represents the emergent part of a ca. 3 km high edifice. The sub-aerial evolution of Stromboli is the result of constructional effusive and explosive activity in the last 100 ka (Paleostromboli, Vancori, Scari, Neostromboli, and Recent Stromboli periods), also coupled with destructive phases of caldera and sector collapses [32–35], whereas the islet of Strombolicchio (the remnant of a volcanic neck) shows an older age of ca. 200 ka (Figure 3a). This volcano is the archetype for Strombolian eruptions and is characterized by persistent activity, mainly consisting of mild intermittent explosions and relative accumulation of high porphyritic (HP) black scoria (shoshonitic basalts with plagioclase + olivine + clinopyroxene phenocrysts/microlites ad cryptocrystalline to glassy groundmass), lapilli and ash near the summit craters, accompanied by constant and abundant degassing [22,36,37]. The HP magma, stored at a relatively shallow depth, can also periodically outpour as lava flows, whereas gas-rich, low porphyritic (LP), and deeper basalt, with whole rock compositions poorly differing from that of the HP scoria, can occasionally erupt during more violent explosive episodes (small and large-scale paroxysms)

as highly vesicular “golden pumices” (from their yellowish-brownish colour) commonly mingled with HP products [37–41].

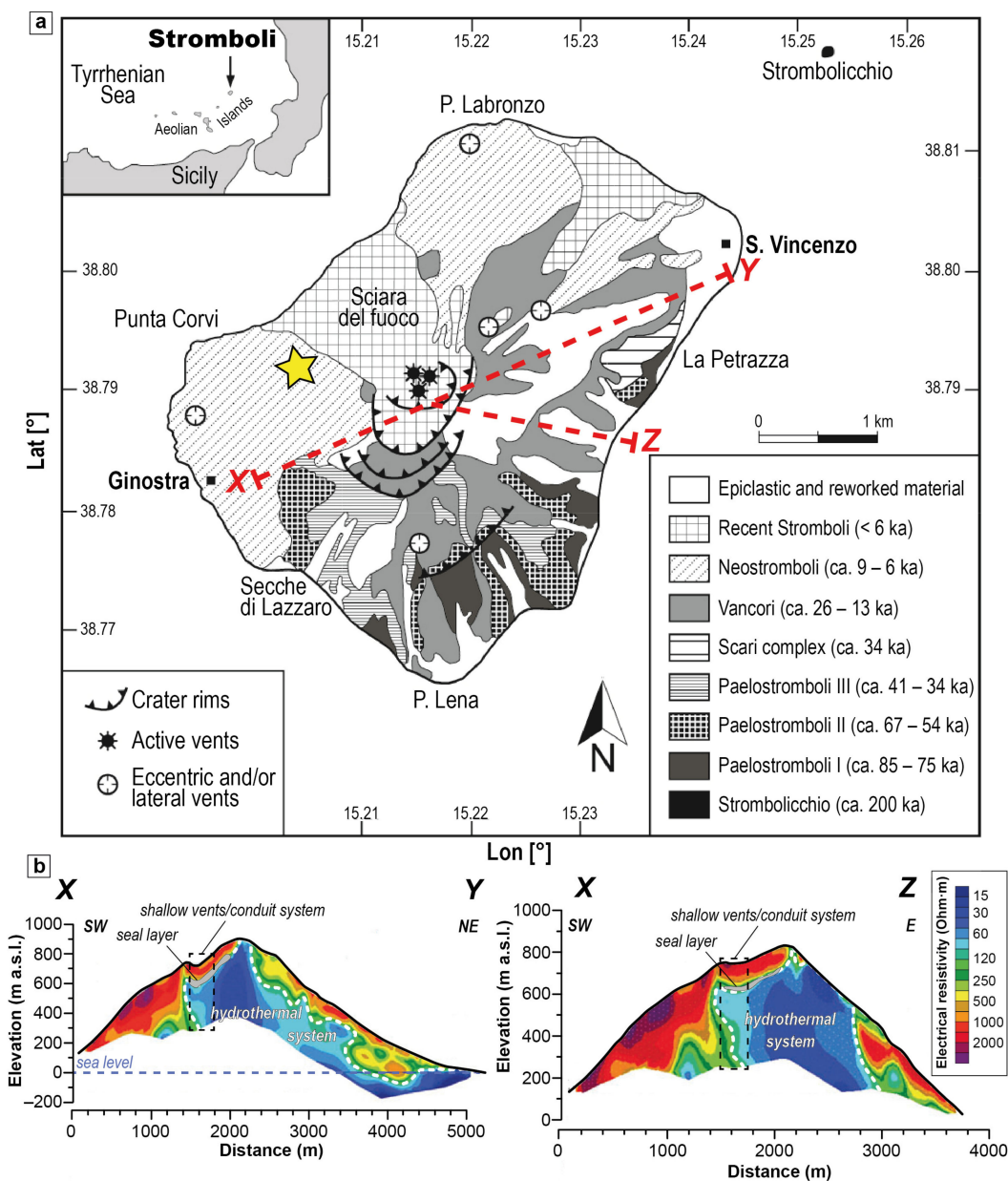


Figure 3. (a) Simplified geological map of the Stromboli volcano (modified after [33]). Neostromboli interval of activity is also in agreement with recent stratigraphic and volcanological reconstruction of Vezzoli et al. [42] and new paleomagnetic datings of Risica et al. [43]. The yellow star indicates the sampling point of the B1 porcellanite–buchite xenolith that was erupted during the 5 April 2003 paroxysm of Stromboli; red dashed lines represent the cross-sections X–Y and X–Z reported in (b); Lat [°] and Lon [°] stand for Latitude and Longitude in decimal degrees, respectively (coordinate system WGS84); (b) DC resistivity tomograms (in ohm·m) along two profiles of Stromboli volcano (X–Y and X–Z) emphasize the extension of the hydrothermal system outlined by low values (15–50 ohm·m) of electrical resistivity (redrawn from [44]). The shallow vents/conduit system is emphasized by a dashed rectangle, it being the place where the igneous pyrometamorphic processes of Stromboli, as those described for the investigated B1 xenolith, may commonly occur.

Stromboli mantle-derived basaltic magmas rise into a thinned continental crust, which, according to geophysical investigations, is defined by a Moho located at a depth of 14.8 km, where S-wave mantle velocities reach 4.0 km/s [45]. Several authors have suggested the presence of at least two crustal levels of storage and crystallization of magmas in the

present-day magma plumbing system of Stromboli [29,31,38,39,46,47]: a deeper reservoir located between 6–7 and 9–11 km, refilled by ascending mantle-derived basaltic magmas and then rising as LP basalts, and a shallower zone at depth <3 km (HP basalts) that feeds the persistent mild explosive activity.

The study of a wide range of undeformed mafic cumulates and mylonitic gabbro cognates [48–50], monzonites [51,52], dolerites [53], intrusive, contact metamorphic to pyrometamorphic xenoliths [17,21,54–58] within Stromboli's subaerial extrusive rocks strongly enhanced understanding of the volcanic plumbing system from deep to shallow levels. Investigations of partially melted felsic intrusive xenoliths of Stromboli also emphasized similarities with the granitoids and metapelite–quartzite sequences of the Calabria–Peloritani arc [55]. All of the above lithologies represent the magma–wall rocks of the Stromboli magmatic plumbing system from the deeper to the shallower crustal levels, including through the volcano cone where the magma conduit wall rocks are instead represented by subvolcanic lithologies and extrusives of the edifice itself and their hydrothermally-altered counterparts.

2.1. Stromboli Degassing and Hydrothermal System

The crater area of Stromboli is affected by continuous gas emission (e.g., [59–61]). The visible surface expression of passive degassing of the magma, resulting from the open–vent system, coexists with active degassing [62] associated with either (i) explosions and (ii) puffing, this latter being the typical degassing mode of the volcano and consisting of the emission of small over-pressurized gas jets/pockets [63]. The volcano continuously degasses SO₂ at rates from about 150 to over 600 t·d^{−1} [59] and from a few hundred to more than 10,000 t·d^{−1} of CO₂ [60] depending upon the periods of activity of the volcano. The compositional features of Stromboli's gas emissions result from the mixing of gases continuously sourced by (i) degassing of dissolved volatiles in the porphyritic magma filling the uppermost dyke–conduit system and (ii) CO₂–rich gas bubbles, originating at depths >4 km (P > 100 MPa) of the plumbing system. Changes in magma convection rate or gas content and/or a structural/tectonic control on the rate of gas bubble supply from depth are considered at the base of the striking variability in Stromboli's gas emissions [60]. The overall composition of the gas emitted by Stromboli, ignoring minor components, is dominated by H₂O (48–98 mol%; mean 80%), CO₂ (2–50 mol%; mean 17%) and SO₂ (0.2–14 mol%; mean 3%) [64], closely resembling the typical composition of volcanic gases from arc-settings, though sharing with nearby Etna volcano a characteristic of CO₂ enrichment [65]. Halogen concentrations (HCl, HF) in volcanic gas appear to vary with respect to SO₂ and CO₂ as a function of stages in the eruptive cycle [66].

The shallow active hydrothermal system of Stromboli has been studied by many authors (e.g., [44,61,67–72]) via temperature, spontaneous potential field anomalies, CO₂ emissions' measurements, and passive seismic studies monitoring. This hydrothermal system, highlighted by a conductive body with electrical resistivity in the range 15–50 ohm·m, is located in the central part of the volcanic edifice with an extension in both the northeast and east directions (Figure 3b) [44].

While many data are available on the volcanic gas composition and emission rates of volcanic gas and gaseous discharge from the hydrothermal system of Stromboli, the only published data, to the best of our knowledge, on Stromboli fumarolic encrustations and sublimates are from Coradossi and Corsini [73]. These authors found: (i) aragonite deposits in the relatively low-T fumarolic zone, (ii) gypsum, anhydrite and pickeringite (magnesium aluminum sulphate) as sublimates from medium-T steam emissions, and (iii) salammoniac, halite, sylvite and alunite in the highest-T fumaroles. Anhydrite precipitation, both in vesicles and as rims of clinopyroxenes (thicknesses on the order of tens of μm) together with orthopyroxene, magnetite and silica–rich glass, were also found in lapilli tuff ejecta of Stromboli [22] as the result of SO₂ gas reaction with clinopyroxene phenocrysts. Anhydrite derived by the degassed SO₂ reactions with diopside at high temperatures (>600 °C) was experimentally demonstrated by Li et al. [74].

2.2. Stromboli Hydrothermal-Rock Ejecta

In the hydrothermally-altered ejecta of Stromboli that experienced weak to moderate alteration, the original porphyritic texture of the Stromboli volcanic rocks is still clearly recognizable [21]: mafic phenocrysts are oxidized and feldspars have not experienced a high degree of dissolution or alteration. XRD analyses of these ejecta show the presence of Ca-sulphate or hydrous Ca-sulphate, cristobalite and hematite [21], and mass-balance calculations performed using the isocon method [75,76] revealed some depletion in major and trace elements, compared with fresh shoshonitic basalt. By contrast, in some hydrothermally-altered basaltic scoria and lava ejecta, the original porphyritic texture is almost completely obliterated, pseudomorphic phenocrysts can be barely recognized, and glass is almost entirely replaced by secondary phases, mainly Mg, Al and Na hydrous sulphate or hydroxysulphate minerals, precipitated during hydrothermal leaching of the extrusive or subvolcanic rocks. The whole-rock chemistry of these strongly hydrothermally-altered volcanics [21] is in agreement with the recognized mineral phases, showing a general depletion in major oxides with the exception of those that are major constituents of the secondary mineral phases (Mg, Al, Na, S, Cl, F). Veins and zones of cristobalite and amorphous silica can also be observed at the micro-mesoscale.

Some of these ejecta can be considered true fumarolic incrustations and sublimates (similar to those investigated by Coradossi and Corsini [73]) due to exposure to oxidized volcanic gas in solfatara, while others are hydrothermally-altered volcanic and subvolcanic rocks of the Stromboli edifice belonging to the intermediate argillic, advanced argillic or silicic alteration [77,78], likely representing the rocks of the shallow hydrothermal zone of the volcano which could interact subsurface with the rising basaltic magmas of the volcano. These kinds of hydrothermal ejecta are considered the aluminum-enriched early protoliths of some igneous pyrometamorphic ejecta of Stromboli [21,22].

3. Materials and Methods

The unique sulphide-rich composite porcellanite–buchite B1 xenolith (Figure 2) erupted as a fragment during the 5 April 2003 paroxysm of Stromboli [79] and was sampled as a loose block on the surface by Antonella Bertagnini (INGV—Istituto Nazionale di Geofisica e Vulcanologia, Italy) at ca. 400 m of altitude in the western part of the island, NE of Ginostra village (Figure 3a). In this paroxysm, several lithic blocks erupted, mainly lavas and subvolcanic dolerites [53], these latter often coated with the LP pumices, the main juvenile component, and the HP scoria.

Although already investigated by Del Moro et al. [21], the B1 sample—mainly termed as a cordierite–plagioclase facies by these authors—deserved to be further studied because of the distinctive occurrence of sulphide globules. White porcellanite and dark buchite that intimately mingled each other suggested a working hypothesis of complex multistage igneous pyrometamorphic events coupled with high temperature mineral–gas reactions. The tridymite–clinopyroxene facies in the B1 composite xenolith, mentioned by Del Moro et al. [21], corresponds to negligible parts of the sample and is therefore beyond the scope of the present paper. In this work, quantitative spot analyses of discrete minerals and glasses were carried out by a Hitachi 4300 FESEM (Hitachi, Schaumburg, IL, USA) equipped with an Oxford Instruments INCA EDS analyser with a spatial resolution of about 3 to 5 μm . The relative analytical error for major elements in Table 1 is 1–2%. The system was calibrated against well characterised reference minerals (Astimex). QEMSCANTM (Quantitative Evaluation of Minerals by Scanning Electron Microscopy) mineral and element mapping were undertaken at the Centre for Advanced Microscopy at the Australian National University using a FEI QEMSCANTM automated SEM–EDS system on polished samples (for analytical methods, see Sieber et al. [80]). Some bulk rock and mineral analyses of B1 xenolith are taken from Del Moro et al. [21], where analytical methods and standards can also be found.

Table 1. FESEM EDS analyses of porcellanite glass (PG) and buchite glass (BG) of B1 xenolith. The three last columns represent the reference composition of the three glasses' population (mean) of the glass (using 2 μm spots) for the QEMSCANTM map of Figure 4: PG*: porcellanite glass mean population; HSG1*: High silica glass, mean population 1 in the buchite; HSG2*: High silica glass, mean population 2 in the buchite.

Oxide	PG	PG	PG	PG	PG	PG	PG	BG	BG	BG	BG	BG	BG	BG	BG	BG	PG*	HSG1*	HSG2*
SiO ₂	55.1	54.5	54.4	53.3	52.9	50.7	50.5	79.7	77.5	74.7	69.6	67.5	66.0	63.0	61.0	53.4	77.7	65.9	
TiO ₂	0.28	0.57	0.42	0.32	0.46	0.33	0.33	0.55	0.51	0.96	0.32	0.49	0.40	0.55	1.26	0.32	0.52	0.68	
Al ₂ O ₃	37.3	37.3	38.0	39.0	39.3	42.2	42.3	11.1	13.0	14.2	17.0	17.3	20.8	19.0	20.1	39.0	13.0	18.7	
FeO _{tot}	0.92	1.02	0.85	0.88	1.03	0.85	0.94	0.64	1.04	0.97	1.75	1.46	2.20	2.78	2.07	0.87	1.04	1.26	
MgO	0.23	0.34	0.56	0.33	0.49	0.27	0.32	0.20	0.24	0.33	0.41	0.64	3.27	1.78	1.22	0.33	0.23	0.70	
CaO	0.49	0.49	0.43	0.59	0.52	0.53	0.57	0.37	0.60	0.74	0.92	0.69	0.69	1.46	1.42	0.59	0.60	0.91	
Na ₂ O	1.56	1.51	1.46	1.48	1.50	1.42	1.41	1.91	1.42	1.81	2.39	3.63	1.68	4.03	4.29	1.48	1.42	3.94	
K ₂ O	3.70	3.76	3.53	3.65	3.45	3.17	3.21	5.54	5.30	5.94	5.99	7.60	4.40	7.16	7.23	3.65	5.30	7.70	
P ₂ O ₅	0.41	0.48	0.30	0.46	0.30	0.50	0.48	-	0.35	0.37	0.80	0.55	0.57	0.23	1.41	-	-	-	
SO ₃	-	-	-	-	-	-	-	-	-	-	0.84	0.18	-	-	-	-	-	-	
Total	99.99	99.97	99.95	100.01	99.95	99.97	100.06	100.01	99.96	100.02	100.02	100.04	100.01	99.99	100	99.64	99.81	99.79	

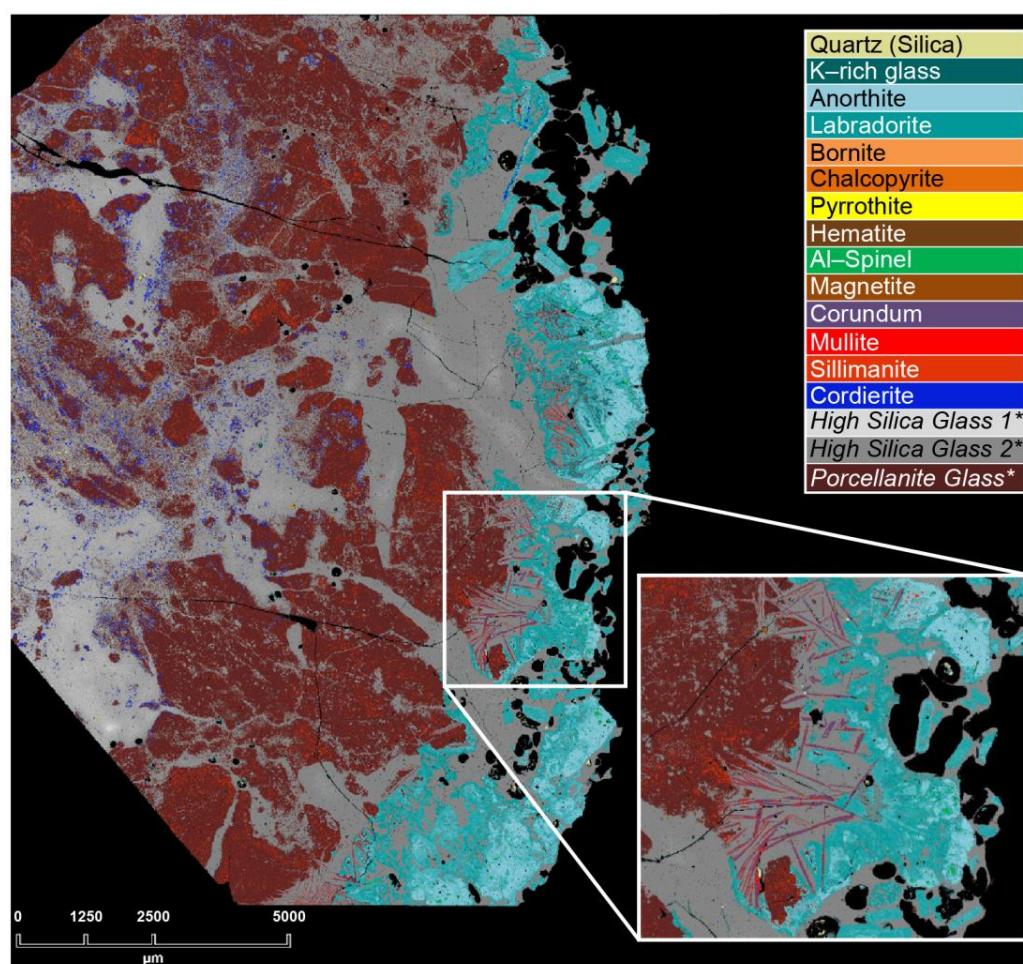


Figure 4. A large (1.25 cm \times 1.75 cm) QEMSCANTM area (step from one pixel to the next is 4.8 μm) of the composite porcellanite–buchite xenolith (B1). The inset highlights the acicular needles that change from corundum to mullite, Al–spinel and high An% plagioclase + glass marking the contact between the xenolith (**left**) and the LP–HP basaltic magma (to the **right**, not present in this figure). The anorthite–labradorite colour indices provide the plagioclase composition between these end-members for both phenocrysts and glass.

The distribution of sulphide globules in a 5 mm diameter core of B1 was also mapped by high resolution (2.3 μm voxel) X-ray μCT using custom facilities in the Department of Applied Mathematics at the Research School of Physics and Engineering at the Australian

National University. Results are provided in the Supplementary Materials (Video S1: 3D data visualization of the X-ray μ CT investigation on a 5 mm diameter core of the porcellanite–buchite sample; Table S1: sulphide globules size and abundance distribution).

4. Results

4.1. Mineral Phases and Glass Compositions

The composite porcellanite–buchite sample B1 is a cryptocrystalline to glassy pyrometamorphic rock where cordierite, mullite/sillimanite, aluminous spinel and corundum represent the main recognized silicate and oxide minerals [21], together with abundant sulphide globules. With respect to analysis of the context of the evolution of the composite xenolith, it is important to note that the basalt coating the xenolith is represented by the two juvenile magmas commonly erupted during paroxysmic eruptions of Stromboli, namely LP and HP basalts (Figure 2). In the high resolution QEMSCANTM map of Figure 4 (ca 1.25 cm \times 1.75 cm) that shows the distribution of mineral phases (as colour variations) across the B1 sample, the main silicates, oxides and sulphides are emphasized, and it is evident that most of the xenolith consists of silicate glass.

Based on quantitative EDS analyses using spots selected in order to minimise the inclusion of nano scale mullite crystals, the glass compositions were roughly subdivided (Table 1; Figure 4), on average, into: (i) lower silica porcellanite glass (*PG**) also crowded by micro-nano mullite and sillimanite and consisting of 53.4 wt.% SiO₂ and 39.0 wt.% Al₂O₃, (ii) higher silica glass 1 (*HSG1**) in the buchite portions and characterized by 77.7 wt.% SiO₂ and 13.0 wt.% Al₂O₃ and (iii) higher silica glass 2 (*HSG2**) always characterizing the buchite, showing 65.9 wt.% SiO₂ and 18.7 wt.% Al₂O₃. Necessarily, the overall composition of the evolved melts would have been higher in Al₂O₃ given the crystallization of abundant mullite within the evolved glass. It is worth noting that the total oxide concentration near 100% in Table 1 could be explained by water driven off at the very high temperature (≥ 1000 °C) and therefore almost entirely lost. The efficiency of such loss could be due to the open-system process (see next Chapters). Moreover, the abundance of micro-crypto crystalline mullite precluded satisfactory ICP–MS spot analyses of glass.

As commonly found in high-T low-P pyrometamorphic rocks [81,82], cordierite is characterized by a peculiar high K₂O content (0.2–1.2 wt.%; [21]) and is mostly concentrated in the higher silica glass of the buchite. As investigated by Del Moro et al. [21], all the crystals of cordierites studied show orthorhombic symmetry, although a transformation from precursor hexagonal indialite is considered likely.

The white porcellanite and dark buchite should be considered as distinct rock domains of the sample. A very thin crystalline to glassy selvage (previously defined as mullite–plagioclase palisade by Del Moro et al. [21]) made of acicular mullite–corundum, aluminous spinel and plagioclase + glass, marks, to a depth of maximum 4 mm (Figure 4), the contact with the juvenile basalt mantling the ejecta. Spinel in the selvage have lower Al₂O₃ (43.7–63.9 wt.%) and higher FeO_{tot} (18.8–38.8 wt.%) with respect to those in the porcellanite–buchite main xenolith (Al₂O₃ 59.9–64.0 wt.%; FeO_{tot} 12.3–12.4 wt.%) [21]. This can be the result of Fe-enrichment by diffusion processes from the basaltic magma at the contact with the xenolith. As shown in Figure 4, plagioclase in the selvage, forming tabular and prismatic crystals up to 500 μ m in length, is characterized by a relatively high content of anorthite (from An₈₂ to An₉₂; [21], mostly emphasized as labradorite or anorthite in Figure 4) and FeO_{tot} 0.5–2.3 wt.%. The relatively high to very high Al-content throughout the composite xenolith is highlighted in Figure 5a, whereas the crystalline to glassy selvage at the contact with the main porcellanite–buchite is characterized by a strong Ca enrichment and a relatively high content of Fe with respect to Mg (Figure 5b–d).

Intergrown low- and high-Cu pyrrhotite and chalcopyrite were detected and mapped within sulphide globules in Figures 4, 6 and 7. These sulphide globules only crowd the buchite portion of the composite ejecta, and this is very well shown in Figure 6a,b and Figure 7a where the bright sulphide globules in the FESEM backscatter images are absent in the porcellanite portions. This distribution clearly links the sulphide formation to a

distinct petrogenetic stage of the evolution of the composite xenolith during the formation of the higher-silica glass. FESEM images of the sulphide globules on the surface of shards of B1 sample in the buchite portion are shown in Figure 6c–d. According to high resolution X-ray μ CT imaging (Figure 8a and Video S1) performed on a 5 mm diameter core of the porcellanite–buchite xenolith, about 1.1 million of sulphide globules (>99.5%) range from <2.5 to 1600 μ m in diameter although more than 50% have diameters <34.5 μ m (Table S1). The two porcellanite and buchite glasses are immiscible as evidenced by the slightly angular, cusped–convolute margins between them, suggesting a liquid–liquid interaction (Figures 2, 4, 6 and 7).

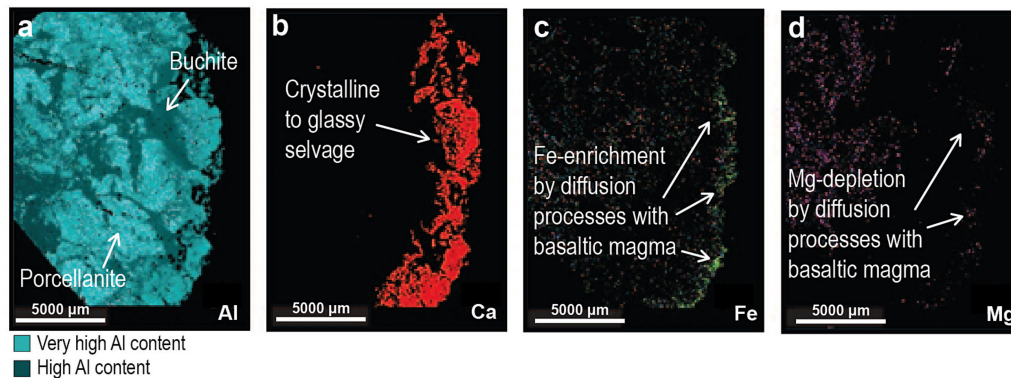


Figure 5. QEMSCAN™ element maps showing relative element concentrations (a) Al, (b) Ca, (c) Fe, and (d) Mg colour variations across the mapped region of B1 shown in Figure 5.

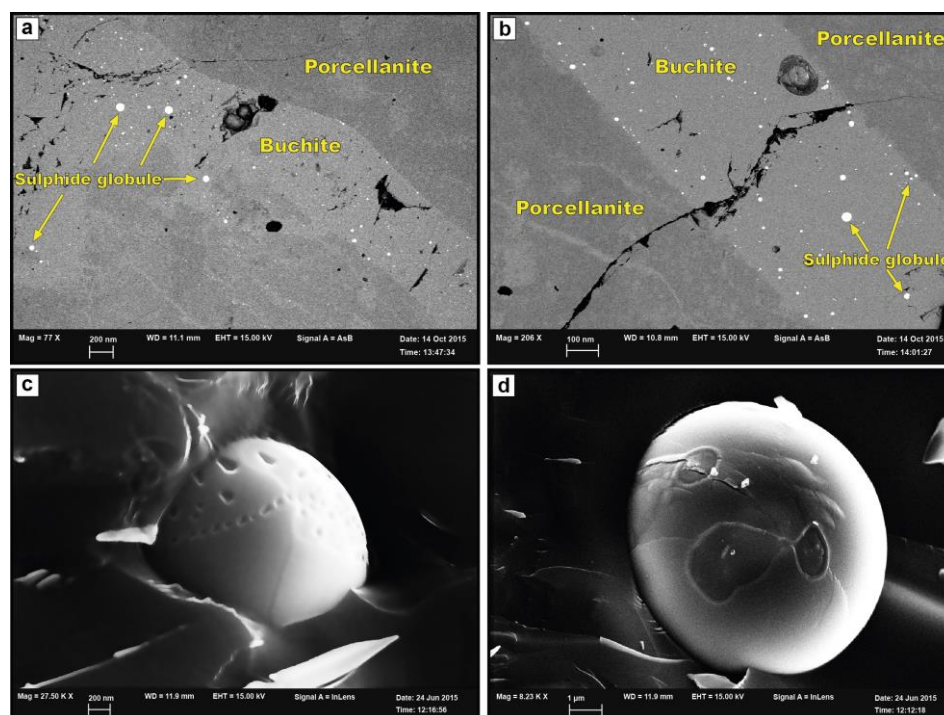


Figure 6. FESEM backscattered image of the composite B1 xenolith at lower (a) and higher (b) magnification, showing intimately mingled porcellanite and buchite. The two portions of the pyrometamorphic xenolith are also distinguished by the presence of sulphide globules only in the buchite portions as further emphasized in the X-ray μ CT imaging provided in Figure 8a and Video S1. Sharpened FESEM images of sulphide globules exposed on the surface of a buchite glass shard from sample B1, having a size of about 2 μ m and 8 μ m are shown in (c) and (d), respectively.

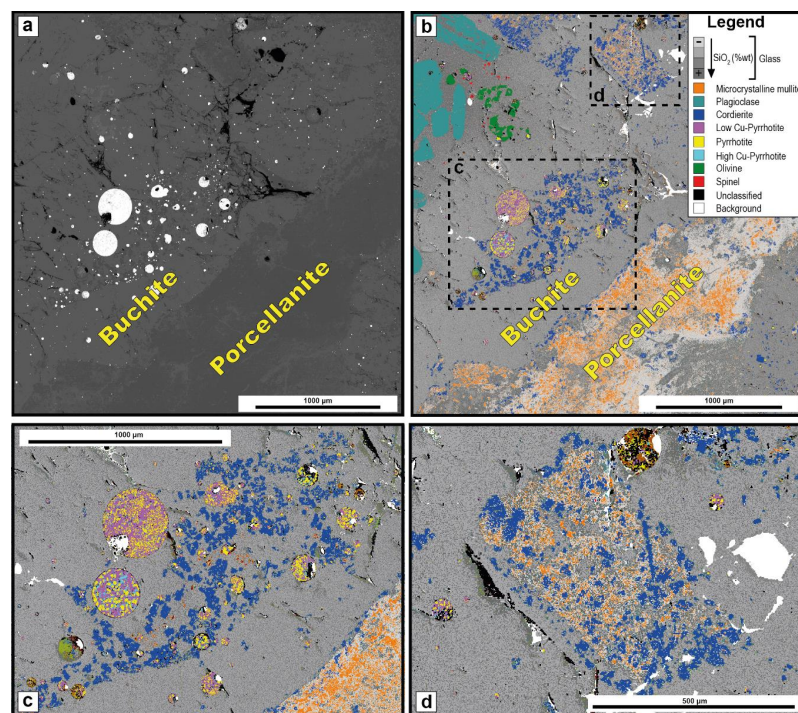


Figure 7. Backscatter FESEM image with the bright sulphide globules in the buchite portion (a); QEMSCANTM map (step size of one pixel to the other is 1.3 µm) of the B1 porcellanite–buchite composite xenolith (b); close-up of the QEMSCANTM map (buchite portions): sulphide globules (pyrrhotite, Low-Cu pyrrhotite and High-Cu pyrrhotite) (c); pseudomorphous clinopyroxene of the early protolith of the xenoliths mainly replaced by cordierite and mullite (d). For abundance and size distribution of the sulphide globules, see also X-ray µCT scan data in Figure 8a and presented in the Supplementary Materials (Video S1, Table S1).

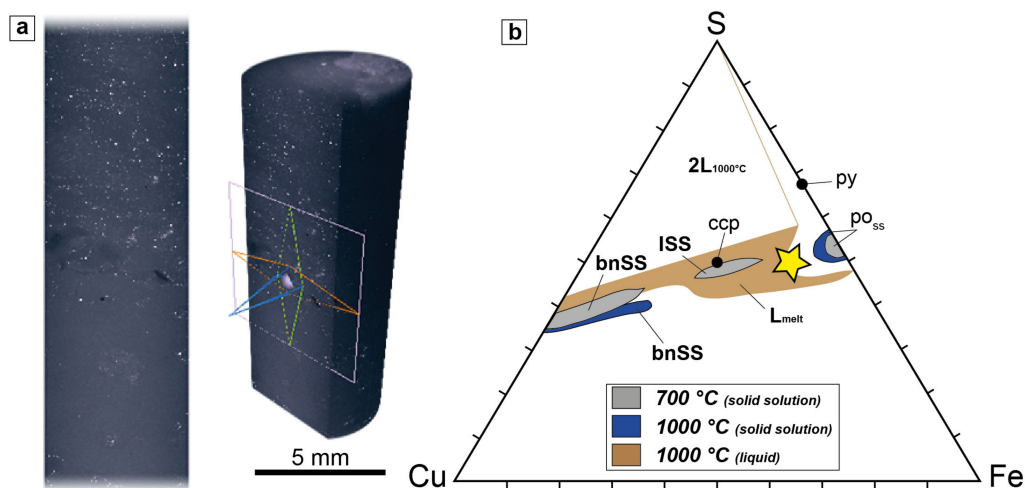


Figure 8. (a) Slices of the composite porcellanite–buchite xenolith of Stromboli through the 3D X-ray µCT data for a 5 mm diameter core (high resolution 2.3 µm voxel size). They show the sulphide globules (as bright spots) in xz planes as we see flying through the 3D data in the video (see Video S1) where their abundance is far larger than how it appears on a 2D polished section surface due to steric effects (polished sections only expose minerals at a single surface so that fine particles beneath the immediate surface are not visible); (b) phase relations in the Cu–Fe–S system at 700 °C and 1000 °C from Vaughan and Craig [83] adapted from Barton and Skinner [84]. L = liquid; SS = solid solution; bn = bornite; ISS = intermediate solid solution; py = pyrite; po = pyrrhotite; ccp = chalcopyrite. The yellow star is the approximate bulk composition of the sulphide globules quenched as immiscible liquid in the buchite portion of the B1 xenolith. The composition of the sulphide globules corresponds to a theoretical pyrrhotite–chalcopyrite tie line.

Mineral phases, different glass compositions and the sulphide globules distribution in the B1 sample are also shown by the QEMSCANTM mineral maps of Figure 7b–d, where the increasing silica content in the glass is shown by different grey scale values as verified by EDS spot analysis for sites as free as possible from mullite microcrystals that developed during glass quenching. The porcellanite has much lower SiO₂ and higher Al₂O₃ much denser mullite distribution with respect to the buchite and contains no sulphide globules. Strong depletion of divalent ions (FeO, MgO, CaO) from the glass occurs with increasing silica (Table 1). In the buchite part of the xenolith, Na₂O concentration ratios relative to Al₂O₃ have a wide range exceeding those of the porcellanite, while K₂O in the higher silica glass is strongly enriched (Table 1). The higher-silica glass also contains dispersed microcrystals of mullite but at much lower abundance than in the porcellanite. A pseudomorphic clinopyroxene phenocryst of the early protolith of the xenolith is emphasized in Figure 7d, almost completely replaced by cordierite and mullite.

Pyrrhotite, low-Cu pyrrhotite and high-Cu pyrrhotite occur together within the sulphide globules (close-up of Figure 7c). In detail, they consist of a three-composite phase of cupriferous Fe–S containing, respectively, 1–4, 8–9 and 21–30 mole% Cu. Element mapping data integrated over the two-dimensional cross section of the larger globules gives 10.5 mole% Cu and 39.5 mole% Fe that may be taken as a first estimate of the unmixed original globule composition. Zinc is the only other significant element up to 1 mole%. Some globules are embayed with irregular coatings containing Pb and As sulphide. Unmixing of the sulphide phases to grain sizes less than laser-ablation spot size (20 µm) precluded use of this method to quantify the partitioning of metals between the globules and the surrounding glass. The abundance of sulphide globules is not fully expressed in a 2D polished section due to steric effects (Figure 8a) but becomes very clear in a video of the X-ray µCT scan of 3D data (Video S1).

The ternary sulphide phase diagram (Figure 8b) suggests that, for an initial sulphide molar composition of Cu:Fe:S = 10.5:39.6:49.9 mole% such as that found for some of the Cu–pyrrhotite, the globule temperature was close to 1000 °C. Following the experimental data of Vaughan and Craig [83] for the Cu–Fe–S system (Figure 8b) at 700 °C, melts are entirely quenched to an exsolution assemblage comprising an intermediate solid solution phase (ISS) and chalcopyrite (ccp) and other phases close to CuFeS₂ and a solid solution around bornite (bnSS). By contrast, at 1000 °C, the Cu–Fe–S system is dominated by the presence of an extensive field of a single sulphide liquid crossing the central part of the ternary diagram (Figure 8b). The inferred sulphide molar composition of the globules found in the pyrometamorphic ejecta B1 is close to the limit of the Cu–poor end member liquid at 1000 °C. In this way, the spherical form of the globules and phase unmixing indicate that the sulphides were originally molten in the silicate melt.

4.2. Major and Trace Elements Bulk Rock Composition

Bulk-rock compositions reported by Del Moro et al. [21] for the B1 xenolith show an increase of SiO₂ (56 to 68 wt.%), Na₂O (1.5 to 1.9 wt.%), K₂O (3.6 to 4.7 wt%) and sulphur (0.1 to 0.3%), and a decrease of Al₂O₃ (34 to 19 wt.%) from the white porcellanite to the dark buchite. This is also demonstrated by a bulk rock analysis [21] performed from a mixture of the composite white porcellanite and dark buchite (M–PB) showing an intermediate major element composition. Thus, a relatively high-Al low-Si white porcellanite (HALS–WP) and low-Al high-Si (LAHS–DB) dark buchite can be clearly defined. This agrees with the glass compositions recognized here (Table 1; Figures 4 and 7). Low CaO (0.7–1.0 wt.%) characterize both HALS–WP and LAHS–DB. As reported by Del Moro et al. [21], REE and incompatible trace element patterns (respectively normalized to chondrites and primordial mantle) of the B1 xenolith mostly match the composition of the trachytes of the Upper Vancori that may have undergone hydrothermal leaching prior to burial Neostomboli and Recent Stromboli volcanics.

In the ternary diagram of Figure 9, the buchite suite from Del Moro et al. [21] is entirely distributed within a wide spectrum of hydrothermal alteration, namely intermediate-

advanced argillic, phyllic-propylitic and silicic, taken as reference from Vulcano Island, in the same Aeolian Archipelago (and same subduction-related volcanism) to which Stromboli Island belongs [77]. Bulk rock and glass compositions of the B1 porcellanite–buchite xenolith follow a linear trend between the SiO_2 and $(\text{Al, Fe})_2\text{O}_3 + (\text{Na, K})_2\text{O}$ components and show the same values of $(\text{Fe} + \text{Mg} + \text{Mn} + \text{Ca})\text{O} + \text{TiO}_2 + \text{P}_2\text{O}_5$. The chemical trends of the B1 xenoliths in Figure 9 could therefore be the result of the protolith signature (lavas or pyroclastics of Stromboli which suffered hydrothermal leaching) and the magmatic processes of the open system igneous pyrometamorphism leading to protolith transformation. By contrast, bulk–rock and glass compositions of the Stromboli buchites interpreted as deriving from deeper continental crust [17] show an increasing trend of $(\text{Fe} + \text{Mg} + \text{Mn} + \text{Ca})\text{O} + \text{TiO}_2 + \text{P}_2\text{O}_5$, decreasing SiO_2 and relatively uniform $(\text{Al, Fe})_2\text{O}_3 + (\text{Na, K})_2\text{O}$.

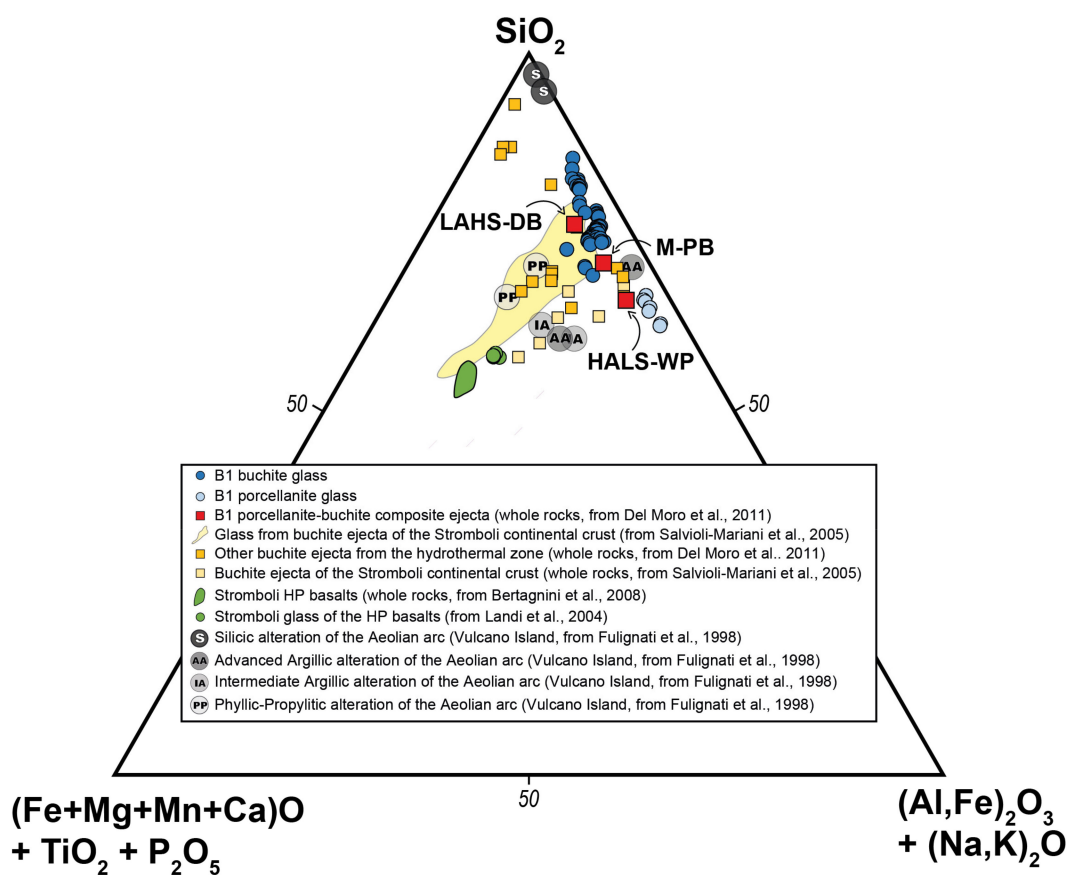


Figure 9. Ternary diagram (from Grapes [1]) of the major element oxides in mol.% for bulk rock compositions and glass of the investigated porcellanite–buchite xenolith (B1) and the buchite suites from Del Moro et al. [21] and Salvioli-Mariani et al. [17]. The B1 porcellanite–buchite composite sample is highlighted with its three analyses (end members HALS–WP, LAHS–DB and the intermediate composition M–PB). Data from Stromboli HP basalt whole rocks [37] and glass [85] are also reported for comparison.

5. Discussion

A unique mineralogical feature of the investigated composite porcellanite–buchite xenolith, B1, from Stromboli is the presence of abundant sulphide globules (pyrrhotite–chalcopyrite). Their occurrence is incompatible with the estimated oxygen fugacity of the LP basalts (between $\text{NNO} + 0.5$ and $\text{NNO} + 1$ [28–31]) and with the oxidizing condition of the shallow acid–sulphate hydrothermal system of the volcano. Sulphide globules were previously recognized in other buchite ejecta of Stromboli [17] but never detected in the HP basalts or their shallow subvolcanic counterparts, i.e., the dolerites. In these latter, however, both Ti-magnetite and ilmenite are present [53], and therefore an oxygen fugacity slightly lower than that of the LP basalt can be inferred.

Sulphate minerals (nor elemental sulphur) are not present in the B1 xenolith so that sulphide formation is not a consequence of a disproportionation reaction. Development of immiscible sulphide melt from a precursor assemblage relatively poor in sulphur requires addition of sulphur from volcanic gas to maintain a gas-saturated melt and reduction of the dissolved SO_2 to S^{-2} . We thus suggest that the sulphide globules are the product of open-system reaction between the evolving xenolith melt and the high flux of magmatic gas interacting with exposed altered Vancori volcanics. Magmatic gas at Stromboli, as for other basaltic volcanoes, is a mixture dominated by H_2O and high in CO_2 , SO_2 , H_2 and HCl , with H_2S as a minor component of the total sulphur [27,64]. These gases are soluble in basaltic melts [86] so that, in an open vent system, the xenolith–basalt melt phase may be considered to have been maintained at gas saturation within the chemically and thermally open-system defined by the xenolith and its external basalt–gas flux together with the diffusion of components including calcium and sulphur into and out of the partially melted white porcellanite (possibly through observed cracks), thus forming the dark buchite portions. Cuspate–convolute margins between white porcellanite and dark buchite implies a liquid–liquid interaction, along permeable areas (cracks) of the early porcellanite induced by the flowing HP basaltic magma–gas eruptive mixture. Above 1000 °C, the favourability of a reaction between a flux of high temperature SO_2 and basaltic melt has been demonstrated experimentally (Henley R.W. unpublished data) and similarly for basaltic glasses [87]. Dissolution of plagioclase into the evolving buchite melt releases Ca as a $\text{CaCl}_{\text{melt}}$ species from plagioclase due to incongruent reaction with HCl from the magmatic gas. There is a consequent release of H_2 into the melt with net localized lowering of f_{O_2} coupled with the reduction of dissolved SO_2 that, with the simultaneous Fe release during cordierite formation, drives sulphide formation. The source of Cu for the sulphide melt is paradoxical, given its presence in only trace quantities in the primary xenolith material and the basaltic melt. As discussed elsewhere (e.g., [27]), the common occurrence of copper in immiscible sulphide melts in volcanic systems suggests that it is scavenged along with SO_2 , HCl , etc. from the gas phase as a dissolved component into the xenolith melt. This is supported by the data of Allard et al. [88] for the emission rates of copper and other metals from Stromboli.

We suggest that open-system igneous pyrometamorphism (i.e., transformation driven by both basaltic magma and high-T gas flux) led to the formation of the immiscible sulphide globules. The formation of these latter is spatially and temporally associated with the buchite parts of the composite xenolith: (i) calcium loss from plagioclase phenocrysts and conversion of ferromagnesian minerals to cordierite, (ii) partial melting of the early porcellanite and exposure of the composite xenolith to high-T gas flux in the active basaltic vent system. This final process was however preceded by a complex petrogenetic history including: a) hydrothermal leaching of fresh volcanics at relatively low-T (advanced argillic alteration facies) and b) high-T igneous pyrometamorphism of a hydrothermally-altered protolith, leading to an early porcellanite.

B1 composite xenolith formation may have occurred at typical pyrometamorphic temperatures >1000 °C which were kept high by the constant flux of volcanic gas in conjunction with basalt melt through the vent system [89].

On Stromboli volcano, the volume of the pyrometamorphic ejecta is quite small relative to the volume of erupted basaltic magma and all other types of lithics [22,53]. The presence of pyrometamorphic xenoliths is linked to major explosions or paroxysms of the volcano and is dependent on the fact that one or more events of igneous pyrometamorphism occurred on vent walls before those eruptions that carried the xenoliths up to the surface. Thus, porcellanite or buchite ejecta can be found more frequently in persistently active basaltic volcanoes such as Stromboli (rather than other active volcanos with long or short periods of rest) because the open vent system and the persistent activity creates more chances of (i) high-T magma–wall rock interaction, (ii) spalling of subvolcanic vent system wall rocks and (iii) high-T gas–solid interactions allowing pyrometamorphic xenoliths to be formed and continuously transformed during vent system processes shortly (we infer months) before being erupted.

Space-Time Inferences on the Formation of the Porcellanite-Buchite Xenolith

As the investigated porcellanite–buchite B1 composite xenolith was erupted during the paroxysm of 5 April 2003, the petrogenetic processes leading to its formation are proposed to be spatially and temporally associated with the shallow subvolcanic system of Stromboli, before and during the Stromboli 2002–2003 eruptive crisis, an effusive eruption which lasted six months, from 28 December 2002 to July 2003 [90–92]. The paroxysm [79] occurred while the lava effusion was still in progress in the lower flanks of the Sciara del Fuoco.

With respect to the general two-stage model (initial hydrothermal leaching and subsequent igneous pyrometamorphism) of the pyrometamorphic process proposed by Del Moro et al. [21], the petrogenetic history of the B1 porcellanite–buchite sample is more complex and requires a multistage process (Figure 10).

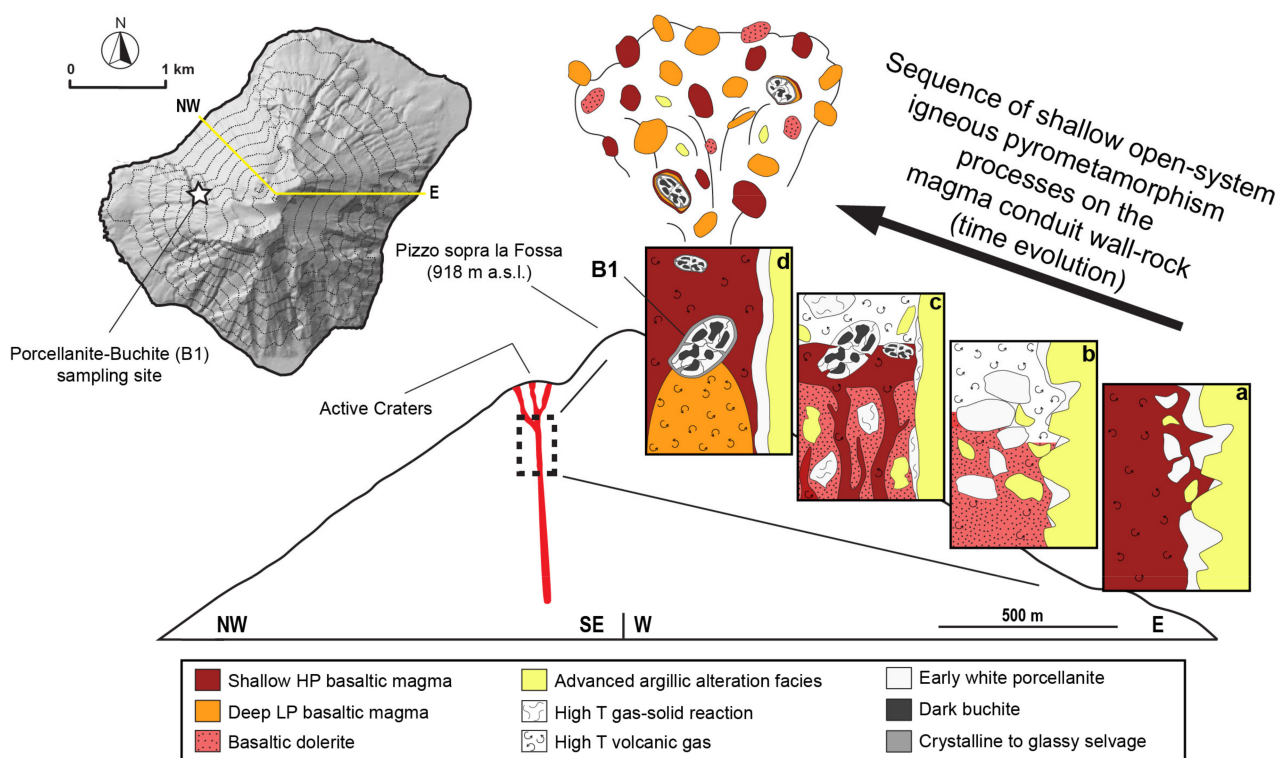


Figure 10. Simplified sketch (in four stages, a–d) explaining the petrogenetic history of the B1 porcellanite–buchite xenolith (erupted during the 5 April 2003 paroxysm, stage d) in the subvolcanic environment of Stromboli volcano. The sketch is envisaged for processes that occurred before (stage a) and during the 2002–2003 eruptive crisis of Stromboli (from January to late March 2003, stages b–c). The 2002–2003 eruptive crisis included an effusive eruption lasting six months (from 28 December 2002 to July 2003; [90,91]) and the violent explosion (paroxysm) that occurred on 5 April 2003 [79] while the lava effusion was still in progress. During this eruptive crisis, the normally persistent summit activity ceased from January to late March 2003, whereas the HP basaltic magmas continued to be outpoured as lavas from vents in the lower flanks of the volcano, along the Sciara del Fuoco [90].

The first stage is the formation of the early porcellanite by igneous pyrometamorphism of magma conduit wall rocks and their spalling off due to the turbulence of the rising HP basaltic magma (Figure 10a), which likely occurred before the 2002–2003 eruptive crisis. The early porcellanite protolith, having high-Al content, could have been porphyritic lavas or pyroclastics of Stromboli affected by an advanced argillic alteration. After the onset of the flank effusive activity on 28 December 2002, the mild strombolian eruptions at the summit crater area ceased until late March 2003 [90,92], although the typical Very Long Period seismicity linked to the gas slugs (generally driving the mild explosions of the persistent activity) continued to be present [91]. As a matter of fact, continuous gas percolation and basaltic dolerite formation were more frequent in the uppermost conduit system during

January–late March 2003 [53]. The presence of (i) abundant miarolitic cavities and (ii) some anomalous metal trace elements in the dolerite ejecta deriving from the shallow crystallization of the HP basalts [53] emphasize the role played by high temperature gas fluxes even during the absence of mild Strombolian eruptions at the crater summit area. In addition, abundant rocks of the vent system engulfed the shallow subvolcanic system at the beginning of the eruptive crisis on 28 December 2002 [92], possibly including porcellanite blocks as well (Figure 10b).

The HP basaltic magma started to intrude again in the uppermost vent system only in late March 2003 (Figure 10c), resuming the persistent crater area activity [91]. During the stages envisaged in Figure 10b,c the early porcellanite may have transformed into a composite xenolith with the developing of the buchite portions enriched in the sulphide globules. The B1 sample was finally ejected together with HP and LP magma, abundant loose basaltic dolerite clasts, doleritic breccias and other type of lithics [53] during the 5 April 2003 paroxystic eruption (Figure 10d).

The thin crystalline to glassy selvage characterized by corundum–mullite needles, Al-spinel and high An% plagioclase between the xenolith and the LP–HP basalt coatings may only represent the very last syneruptive thermometamorphic reaction, just before the xenolith was ejected in the 5 April 2003 paroxysm. Similar selvages are common at the rims of Al-rich xenoliths or pyrometamorphic rocks formed at the contact with basaltic magmas (e.g., [1,93,94]). Bowen [95] was the first to argue that the reaction of an aluminous xenolith with a basic magma would cause excess precipitation of high An% plagioclase from the magma and Preston et al. [94] suggest the reaction:



with clinopyroxene considered the saturated component of the basaltic magma and the Al_2O_3 deriving from the aluminous xenolith.

6. Conclusions

The occurrence of cupriferous immiscible sulphide globules in the investigated pyrometamorphic buchite–porcellanite xenolith from Stromboli is paradoxical, given the general absence of sulphides in the Stromboli erupted basalts. In this paper, we have shown that sulphide globules' formation in the buchite portions of the composite xenolith was coupled with a loss of calcium from plagioclase, pyrometamorphism of ferromagnesian minerals to cordierite–mullite, and melt formation through melting of an early porcellanite deriving from the shallow vents/conduit wall rocks (hydrothermally altered volcanic products). This occurred in the presence of contemporary basalt melt and high-T volcanic gas flux. The loss of Ca emphasizes the open-system context for exchange of reactive gas species between the external volcanic gas flux and the evolving buchite melt. It is suggested that sulphide formation is a consequence of the reaction of HCl dissolved into the melt from the gas phase, Cl stabilization as Ca chloride gas species releasing H_2 into the melt and consequent reduction of dissolved SO_2 . The speciation of sulphur in silicate melts is controversial, but recent advances using X-ray Absorption Near-Edge Spectroscopy (XANES) [96] suggest that increasing FeO content of a melt favours an increase in the S^{2-} concentration. Dissolution of ferromagnesian phenocrysts into the evolving buchite melt coupled with the exchange of SO_2 into the melt from the gas phase then drives the formation of sulphide melts to be quenched as immiscible sulphide globules. Buchite portions of the B1 sample melts are relatively Cu-rich (and often have CuFeS globules), and this suggests that the CuS component of the sulphide globules in the buchite glass may also be due to partitioning of Cu from the gas flux into the melt.

Phase relations and bulk–rock compositions suggest that the evolutionary stages of the porcellanite–buchite assemblages occurred at relatively low pressures (a few tens to hundred bars at most) above 1000 °C and perhaps as high as 1150 °C [1,17,21], commensurate with observed vent temperatures [97] and in agreement with the highest temperature of the igneous pyrometamorphism (Figure 1). This process includes an initial igneous pyrometa-

morphism *stricto sensu* (porcellanite) and subsequent open-system exchange of reactant $\text{SO}_2\text{--HCl--H}_2$ gas and CaCl species between the evolving xenolith melt and the general flux of volcanic gas and basaltic melt (buchite) in the shallow Stromboli vent system. In this way, both a basaltic magma and a gas–flux reaction near magmatic temperature can induce igneous pyrometamorphism (and metasomatism) in a subvolcanic environment through magmatic processes. The B1 composite xenolith has a very complex petrogenesis so that clearer resolution of its components and element zonation patterns (also of additional ejecta of Stromboli derived from open-system igneous pyrometamorphism) awaits further work including experimental determination of relative element diffusivities during reactive mass transfer processes between high temperature gas mixtures and silicate glasses and basaltic magma–xenolith interaction.

Supplementary Materials: The following are available online at <https://www.mdpi.com/article/10.3390/min11060639/s1>, Video S1: 3D data visualization of the X-ray μCT investigation on a 5 mm diameter core of the porcellanite–buchite sample; Table S1: datable Sta on sulphide globules abundance and size distribution.

Author Contributions: Conceptualization, A.R. and R.W.H.; methodology, A.R., M.T., F.J.B., S.D.M. and R.W.H.; materials, S.D.M.; validation, A.R., M.T., F.J.B., S.D.M. and R.W.H.; formal analysis, (X-ray μCT , FESEM and QEMSCAN™ mineral mapping) R.W.H. and F.J.B.; investigation, A.R., M.T., F.J.B., S.D.M. and R.W.H.; data curation, A.R., M.T. and R.W.H.; writing—original draft preparation, A.R., M.T. and R.W.H.; writing—review and editing, A.R., M.T., F.J.B., S.D.M. and R.W.H.; visualization, A.R. and M.T.; supervision, A.R. and R.W.H.; project administration, A.R. and R.W.H. All authors have read and agreed to the published version of the manuscript.

Funding: R.W.H. and F.J.B. note initial funding from the Australian Research Council (Penelope L. King). Department of Pure and Applied Sciences (DISPEA, University of Urbino) financially supported M.T. with a postdoc grant.

Data Availability Statement: All data used in this work are reported in the main text or in the Supplementary Materials.

Acknowledgments: Michael Turner and Hoger Averdunk are thanked for X-ray CT scanning and data processing of the investigated B1 sample. R.W.H. acknowledges the pleasure of being introduced to Stromboli by Volcano Discovery (<https://www.volcanodiscovery.com/>) and thanks Justin Whyte for logistic support. Two anonymous reviewers and Guest Editor of the special issue (Monica Piochi) are thanked for comments and suggestions that really helped to improve an early version of the manuscript.

Conflicts of Interest: The authors declare no conflict of interest.

References

1. Grapes, R. *Pyrometamorphism*; Springer: Berlin, Germany, 2011; 365p.
2. Brauns, R. Die chemische Zusammensetzung granatführender kristalliner Scheifer, Cordieritgesteine und Sanidinite aus dem Laacher Seegebiet. *N. J. Mineral. Geol. Pal.* **1912**, *34*, 85–175.
3. Barton, M.D.; Staude, J.M.; Snow, E.A.; Johnson, D.A. Aureole systematics. In *Contact Metamorphism*; Kerrick, D.M., Ed.; Reviews in Mineralogy, Mineralogical Society of America: Chelsea, MI, USA, 1991; Volume 26, pp. 723–847.
4. Yoder, H.S.; Tilley, C.E. Origin of basaltic magmas: An experimental study of natural and synthetic rock systems. *J. Petrol.* **1962**, *3*, 342–532. [[CrossRef](#)]
5. Tuttle, O.F.; Bowen, N.L. Origin of granite in the light of experimental studies in the system $\text{NaAlSi}_3\text{O}_8\text{--KAlSi}_3\text{O}_8\text{--SiO}_2\text{--H}_2\text{O}$. *Geol. Soc. Am. Mem.* **1958**, *74*, 153.
6. Holdaway, M.J. Stability of andalusite and the aluminium silicate phase diagram. *Am. J. Sci.* **1971**, *271*, 97–131. [[CrossRef](#)]
7. Kennedy, G.C.; Wasserburg, F.J.; Heard, H.C.; Newton, R.C. The upper three-phase region in the system $\text{SiO}_2\text{--H}_2\text{O}$. *Am. J. Sci.* **1962**, *260*, 501–521. [[CrossRef](#)]
8. Ostrovsky, I.A. PT-diagram of the system $\text{SiO}_2\text{--H}_2\text{O}$. *Geol. J.* **1966**, *5*, 127–134. [[CrossRef](#)]
9. Mohl, H. Die südwestlichsten Ausläufer des Vogelsgebirges. *Offenb. Ver. Nat.* **1873**, *14*, 51–101.
10. Tomkeieff, S.I. The dolerite plugs of Tieveragh and Tievebulliagh near Cushendall, Co. Antrim, with a note on buchite. *Geol. Mag.* **1940**, *7*, 54–64. [[CrossRef](#)]
11. Harker, A. *The Tertiary Igneous Rocks of Skye*; H.M. Stationery Office: Glasgow, Scotland, 1904.

12. Thomas, H.H. On certain xenolithic Tertiary minor intrusions in the Island of Mull (Argyllshire). *Q. J. Geol. Soc. Lond.* **1922**, *78*, 229–259. [[CrossRef](#)]
13. Werner, A.G.; Bergm, J. *Traité Élémentaire de Mineralogie I*; Brochant, A.J.M., Ed.; Villier: Paris, France, 1789; 644p.
14. Killie, I.C.; Thompson, R.N.; Morrison, M.A.; Thompson, R.F. Field evidence for turbulence during flow of basalt magma through conduits from southwest Mull. *Geol. Mag.* **1986**, *123*, 693–697. [[CrossRef](#)]
15. Holness, M.B.; Watt, G.R. The aureole of the Traigh Bhàn na Sgùrra Sill, Isle of Mull: Reaction driven microcracking during pyrometamorphism. *J. Petrol.* **2001**, *43*, 511–534. [[CrossRef](#)]
16. Koritnig, S. Die Blaue Kuppe bei Eschwege mit ihren Kontakterscheinungen. *Contrib. Miner. Pet.* **1955**, *4*, 504–521. [[CrossRef](#)]
17. Salviole-Mariani, E.; Renzulli, A.; Serri, G.; Holm, P.M.; Toscani, L. Glass-bearing crustal xenoliths (buchites) erupted during the recent activity of Stromboli (Aeolian Islands). *Lithos* **2005**, *81*, 255–277. [[CrossRef](#)]
18. Balassone, G.; Franco, E.; Mattia, C.A.; Puliti, R. Indialite in xenoliths from Somma–Vesuvius volcano (Southern Italy): Crystal chemistry and petrogenetic features. *Am. Mineral.* **2004**, *89*, 1–6. [[CrossRef](#)]
19. Wood, C.P. Mineralogy at the magma–hydrothermal system interface in andesite volcanoes. *Geology* **1994**, *22*, 75–78. [[CrossRef](#)]
20. Wood, C.P.; Browne, P.R.L. Chlorine-rich pyrometamorphic magma at White Island volcano, New Zealand. *J. Volcanol. Geoth. Res.* **1996**, *72*, 21–35. [[CrossRef](#)]
21. Del Moro, S.; Renzulli, A.; Tribaudino, M. Pyrometamorphic processes at the magma–hydrothermal system interface of active volcanoes: Evidence from buchite ejecta of Stromboli (Aeolian Islands, Italy). *J. Petrol.* **2011**, *52*, 541–564. [[CrossRef](#)]
22. Del Moro, S.; Renzulli, A.; Landi, P.; La Felice, S.; Rosi, M. Unusual lapilli tuff ejecta erupted at Stromboli during the 15 March 2007 explosion shed light on the nature and thermal state of rocks forming the crater system of the volcano. *J. Volcanol. Geoth. Res.* **2013**, *254*, 37–52. [[CrossRef](#)]
23. Fegley, B.; Prinn, R.G. Estimation of the rate of volcanism on Venus from reaction rate measurements. *Nature* **1989**, *337*, 55–58. [[CrossRef](#)]
24. Ayris, P.M.; Lee, A.F.; Wilson, K.; Kueppers, U.; Dingwell, D.B.; Delmelle, P. SO₂ sequestration in large volcanic eruptions: High temperature scavenging by tephra. *Geochim. Cosmochim. Acta* **2013**, *110*, 58–69. [[CrossRef](#)]
25. Henley, R.W.; King, P.L.; Wykes, J.L.; Renggli, C.J.; Brink, F.J.; Clark, D.A.; Troitzsch, U. Porphyry copper deposit formation by sub-volcanic sulfur dioxide flux and gas–solid. *Nat. Geosci.* **2015**, *8*, 210–215. [[CrossRef](#)]
26. Henley, R.W.; Seward, T.M. Gas–Solid Reactions in Arc Volcanoes. Ancient and Modern. *Rev. Mineral. Geochem.* **2018**, *84*, 309–349. [[CrossRef](#)]
27. Henley, R.W.; Fischer, T.P. Sulfur sequestration and redox equilibria in volcanic gases. *J. Volcanol. Geoth. Res.* **2021**, *412*, 107181. [[CrossRef](#)]
28. Métrich, N.; Bonnin–Mosbah, M.; Susini, J.; Menez, B.; Galois, L. Presence of sulfite (S^{IV}) in arc magmas: Implications for volcanic sulfur emissions. *Geophys. Res. Lett.* **2002**, *29*, 1–4. [[CrossRef](#)]
29. Di Carlo, I.; Pichavant, M.; Rotolo, S.G.; Scaillet, B. Experimental crystallization of a high–K arc basalt: The golden pumice, Stromboli volcano (Italy). *J. Petrol.* **2006**, *47*, 1317–1343. [[CrossRef](#)]
30. Pichavant, M.; Di Carlo, I.; Le Gac, Y.; Rotolo, S.G.; Scaillet, B. Experimental constraints on the deep magma feeding system at Stromboli volcano, Italy. *J. Petrol.* **2009**, *50*, 601–624. [[CrossRef](#)]
31. Métrich, N.; Bertagnini, A.; Di Muro, A. Conditions of magma storage, degassing and ascent at Stromboli: New insights into the volcano plumbing system with inferences on the eruptive dynamics. *J. Petrol.* **2010**, *51*, 603–626. [[CrossRef](#)]
32. Francalanci, L.; Manetti, P.; Peccerillo, A. Volcanological and magmatological evolution of Stromboli volcano (Aeolian Islands): The roles of fractional crystallization, magma mixing, crustal contamination and source heterogeneity. *Bull. Volcanol.* **1989**, *51*, 355–378. [[CrossRef](#)]
33. Hornig–Kjarsgaard, I.; Keller, J.; Kobersky, U.; Stadlbauer, E.; Francalanci, L.; Lenhart, R. Geology, stratigraphy and volcanological evolution of the island of Stromboli, Aeolian Arc, Italy. *Acta Vulcanol.* **1993**, *3*, 21–68.
34. Tibaldi, A. Multiple sector collapses at Stromboli volcano: How they work. *Bull. Volcanol.* **2001**, *63*, 112–125. [[CrossRef](#)]
35. Francalanci, L.; Lucchi, F.; Keller, J.; De Astis, G.; Tranne, C.A. Chapter 13, Eruptive, volcano–tectonic and magmatic history of the Stromboli volcano (north–eastern Aeolian archipelago). In *In The Aeolian Islands Volcanoes*; Lucchi, F., Peccerillo, A., Keller, J., Tranne, C.A., Rossi, P.L., Eds.; Geological Society of London: London, UK, 2013; Volume 37, pp. 397–471.
36. Rosi, M.; Bertagnini, A.; Landi, P. Onset of the persistent activity at Stromboli volcano (Italy). *Bull. Volcanol.* **2000**, *62*, 294–300. [[CrossRef](#)]
37. Bertagnini, A.; Métrich, N.; Francalanci, L.; Landi, P.; Tommasini, S.; Conticelli, S. Volcanology and Magma Geochemistry of the Present–Day Activity: Constraints on the Feeding System. In *The Stromboli Volcano: An Integrated Study of the 2002–2003 Eruption, Volume 182*; Calvari, S., Inguaggiato, S., Puglisi, G., Ripepe, M., Rosi, M., Eds.; American Geophysical Union: Washington, DC, USA, 2008; pp. 19–37.
38. Métrich, N.; Bertagnini, A.; Landi, P.; Rosi, M. Crystallization driven by decompression and water loss at Stromboli volcano (Aeolian Islands, Italy). *J. Petrol.* **2001**, *42*, 1471–1490. [[CrossRef](#)]
39. Bertagnini, A.; Métrich, N.; Landi, P.; Rosi, M. Stromboli volcano (Aeolian Archipelago, Italy): An open window on the deep–feeding system of a steady state basaltic volcano. *J. Geophys. Res.* **2003**, *108*, 1–15. [[CrossRef](#)]

40. Rosi, M.; Pistolesi, M.; Bertagnini, A.; Landi, P.; Pompilio, M.; Di Roberto, A. Chapter 14, Stromboli volcano, Aeolian Islands (Italy): Present eruptive activity and hazards. In *The Aeolian Islands Volcanoes*; Lucchi, F., Peccerillo, A., Keller, J., Tranne, C.A., Rossi, P.L., Eds.; Geological Society of London: London, UK, 2013; Volume 37, pp. 473–490.
41. Giordano, G.; De Astis, G. The summer 2019 basaltic Vulcanian eruptions (paroxysms) of Stromboli. *Bull. Volcanol.* **2021**, *83*, 1. [[CrossRef](#)]
42. Vezzoli, L.; Renzulli, A.; Menna, M. Growth after collapse: The volcanic and magmatic history of the Neostromboli lava cone (island of Stromboli, Italy). *Bull. Volcanol.* **2014**, *76*, 821. [[CrossRef](#)]
43. Risica, G.; Speranza, F.; Giordano, G.; De Astis, G.; Lucchi, F. Palaeomagnetic dating of the Neostromboli succession. *J. Volcanol. Geoth. Res.* **2019**, *371*, 229–244. [[CrossRef](#)]
44. Revil, A.; Finizola, A.; Ricci, T.; Delcher, E.; Peltier, A.; Barde–Cabusson, S.; Avard, G.; Bailly, T.; Bennati, L.; Byrdina, S.; et al. Hydrogeology of Stromboli volcano, Aeolian Islands (Italy) from the interpretation of resistivity tomograms, self–potential, soil temperature and soil CO₂ concentration measurements. *Geophys. J. Int.* **2011**, *186*, 1078–1094. [[CrossRef](#)]
45. Martínez–Arevalo, C.; Musumeci, C.; Patanè, D. Evidence of a partial melt zone beneath Stromboli volcano (Italy) from inversion of teleseismic receiver functions. *Terra Nova* **2009**, *21*, 386–392. [[CrossRef](#)]
46. Ubide, T.; Caulfield, J.; Brandt, C.; Bussweiler, Y.; Mollo, S.; Di Stefano, F.; Nazzari, M.; Scarlato, P. Deep Magma Storage Revealed by Multi–Method Elemental Mapping of Clinopyroxene Megacrysts at Stromboli Volcano. *Front. Earth Sci.* **2019**, *7*, 239. [[CrossRef](#)]
47. Métrich, N.; Bertagnini, A.; Pistolesi, M. Paroxysms at Stromboli Volcano (Italy): Source, Genesis and Dynamics. *Front. Earth Sci.* **2021**, *9*, 593339. [[CrossRef](#)]
48. Salvioli–Mariani, E.; Mattioli, M.; Renzulli, A.; Serri, G. Silicate melt inclusions in the cumulate minerals of gabbroic nodules from Stromboli volcano (Aeolian Islands, Italy): Main components of the fluid phase and crystallization temperatures. *Mineral Mag.* **2002**, *66*, 969–984. [[CrossRef](#)]
49. Mattioli, M.; Serri, G.; Salvioli–Mariani, E.; Renzulli, A.; Holm, P.M.; Santi, P.; Venturelli, G. Subvolcanic infiltration and syneruptive quenching of liquids in cumulate wall–rocks: The example of the gabbroic nodules of Stromboli (Aeolian Islands, Italy). *Mineral. Petrol.* **2003**, *78*, 201–230. [[CrossRef](#)]
50. Spiess, R.; Dibona, R.; Faccenda, M.; Mattioli, M.; Renzulli, A. Mylonitic gabbro nodules of Stromboli (southern Italy): Microstructural evidence of high–temperature deformation of cumulates during the evolution of the magmatic crustal roots of an active volcano. *Geol. S. Am. S.* **2017**, *526*, 89–105.
51. Renzulli, A.; Santi, P. Subvolcanic crystallization at Stromboli (Aeolian Islands, southern Italy) preceding the Sciara del Fuoco sector collapse: Evidence from monzonite lithic suite. *Bull. Volcanol.* **1997**, *59*, 10–20. [[CrossRef](#)]
52. Menna, M.; Tribaudino, M.; Renzulli, A. Al–Si order and spinodal decomposition texture of a sanidine from igneous clasts of Stromboli (Aeolian arc, southern Italy): Insights into the timing between the emplacement of a shallow basic sheet intrusion and the eruption of related ejecta. *Eur. J. Mineral.* **2008**, *20*, 183–190. [[CrossRef](#)]
53. Renzulli, A.; Del Moro, S.; Menna, M.; Landi, P.; Piermattei, M. Transient processes in Stromboli’s shallow basaltic system inferred from dolerite and magmatic breccia blocks erupted during the 5 April 2003 paroxysm. *Bull. Volcanol.* **2009**, *71*, 795–813. [[CrossRef](#)]
54. Honnorez, J.; Keller, J. Xenolithe in vulkanischen Gesteinen Aolischen Inseln (Sizilien). *Geol. Rundsch.* **1968**, *7*, 719–736. [[CrossRef](#)]
55. Renzulli, A.; Serri, G.; Santi, P.; Mattioli, M.; Holm, P.M. Original of high–silica liquids of Stromboli volcano (Aeolian Island, Italy) inferred from crustal xenoliths. *Bull. Volcanol.* **2001**, *62*, 400–419. [[CrossRef](#)]
56. Renzulli, A.; Tribaudino, M.; Salvioli–Mariani, E.; Serri, G.; Holm, P.M. Cordierite anorthoclase hornfels xenoliths in Stromboli lavas (Aeolian Islands, Sicily): An example of a fast cooled contact aureole. *Eur. J. Mineral.* **2003**, *15*, 665–679. [[CrossRef](#)]
57. Vaggelli, G.; Francalanci, L.; Ruggieri, G.; Testi, S. Persistent polybaric rests of calc–alkaline magmas at Stromboli volcano, Italy: Pressure data from fluid inclusions in restitic quartzite nodules. *Bull. Volcanol.* **2003**, *65*, 385–404. [[CrossRef](#)]
58. Harlov, D.; Renzulli, A.; Ridolfi, F. Iron–bearing chlor–fluorapatites in crustal xenoliths from the Stromboli volcano (Aeolian Islands, Southern Italy): An indicator of fluid processes during contact metamorphism. *Eur. J. Mineral.* **2006**, *18*, 233–241. [[CrossRef](#)]
59. Burton, M.R.; Caltabiano, T.; Murè, F.; Salerno, G.; Randazzo, D. SO₂ flux from Stromboli during the 2007 eruption: Results from the FLAME network and traverse measurements. *J. Volcanol. Geoth. Res.* **2009**, *182*, 214–220. [[CrossRef](#)]
60. Aiuppa, A.; Burton, M.; Caltabiano, T.; Giudice, G.; Guerrieri, S.; Liuzzo, M.; Murè, F.; Salerno, G. Unusually large magmatic CO₂ gas emissions prior to a basaltic paroxysm. *Geophys. Res. Lett.* **2010**, *37*, L17303. [[CrossRef](#)]
61. Inguaggiato, S.; Jacome Paz, M.P.; Mazot, A.; Delgado Granados, H.; Inguaggiato, C.; Vita, F. CO₂ output discharged from Stromboli Island (Italy). *Chem. Geol.* **2013**, *339*, 52–60. [[CrossRef](#)]
62. Tamburello, G.; Aiuppa, A.; Kantzas, E.P.; McGonigle, A.J.S.; Ripepe, M. Passive vs. active degassing modes at an open–vent volcano (Stromboli, Italy). *Earth Planet. Sci. Lett.* **2012**, *359–360*, 106–116. [[CrossRef](#)]
63. Harris, A.; Ripepe, M. Synergy of multiple geophysical approaches to unravel explosive eruption conduits and source dynamics—A case study from Stromboli. *Chemie Erde* **2007**, *67*, 1–35. [[CrossRef](#)]
64. Aiuppa, A.; Bertagnini, A.; Métrich, N.; Moretti, R.; Di Muro, A.; Liuzzo, M.; Tamburello, G. A model of degassing for Stromboli volcano. *Earth Planet. Sci. Lett.* **2010**, *295*, 195–204. [[CrossRef](#)]
65. Shinohara, H. Excess degassing from volcanoes and its role on eruptive and intrusive activity. *Rev. Geophys.* **2008**, *46*, 1–31. [[CrossRef](#)]

66. Aiuppa, A. Degassing of halogens from basaltic volcanism: Insights from volcanic gas observations. *Chem. Geol.* **2009**, *263*, 99–109. [[CrossRef](#)]
67. Finizola, A.; Sortino, F.; Lénat, J.F.; Valenza, M. Fluid circulation at Stromboli volcano (Aeolian Island, Italy) from self-potential and CO₂ surveys. *J. Volcanol. Geoth. Res.* **2002**, *116*, 1–18. [[CrossRef](#)]
68. Finizola, A.; Sortino, F.; Lénat, J.F.; Aubert, M.; Ripepe, M.; Valenza, M. The summit hydrothermal system of Stromboli: New insights from self-potential, temperature, CO₂ and fumarolic fluids measurements, with structural and monitoring implications. *Bull. Volcanol.* **2003**, *65*, 486–504. [[CrossRef](#)]
69. Finizola, A.; Ricci, T.; Deiana, R.; Barde Cabusson, S.; Rossi, M.; Praticelli, N.; Giocoli, A.; Romano, G.; Delcher, E.; Suski, B.; et al. Adventive hydrothermal circulation on Stromboli volcano (Aeolian Island, Italy) revealed by geophysical and geochemical approaches: Implication for general fluid flow models on volcanoes. *J. Volcanol. Geoth. Res.* **2010**, *196*, 111–119. [[CrossRef](#)]
70. Carapezza, M.L.; Federico, C. The contribution of fluid geochemistry to the volcano monitoring of Stromboli. *J. Volcanol. Geoth. Res.* **2000**, *95*, 227–245. [[CrossRef](#)]
71. Carapezza, M.L.; Ricci, T.; Ranaldi, M.; Tarchini, L. Active degassing structures of Stromboli and variations in diffuse CO₂ output related to the volcanic activity. *J. Volcanol. Geoth. Res.* **2009**, *182*, 231–245. [[CrossRef](#)]
72. Calò, M.; López Mazariegos, E.A.; Tramelli, A.; Orazi, M. Hydrothermal systems characterization of the Stromboli volcano using spatial and temporal changes of the seismic velocities. *J. Volcanol. Geoth. Res.* **2021**, *411*, 107177. [[CrossRef](#)]
73. Coradossi, N.; Corsini, F. La natura mineralogica dei più frequenti prodotti fumarolici dello Stromboli (Isole Eolie) nel periodo 1961–1967. *Atti Soc. Toscana Sci. Nat.* **1968**, *75*, 460–482.
74. Li, E.Y.; Chareev, D.A.; Shilobreeva, S.N.; Grichuk, D.V.; Tyutyunnik, O.A. Experimental study of sulfur dioxide interaction with silicates and aluminosilicates at temperatures of 650 and 850 °C. *Geochem. Int.* **2010**, *48*, 1039–1046. [[CrossRef](#)]
75. Gresens, R. Composition–volume relationships of metasomatism. *Chem. Geol.* **1967**, *2*, 47–55. [[CrossRef](#)]
76. Grant, J.A. The isocon diagram: A simple solution to Gresens' equation for metasomatic alteration. *Econ. Geol.* **1986**, *81*, 1976–1982. [[CrossRef](#)]
77. Fulignati, P.; Gioncada, A.; Sbrana, A. Geologic model of the magmatic–hydrothermal system of Vulcano (Aeolian Islands, Italy). *Mineral. Petrol.* **1998**, *62*, 195–222. [[CrossRef](#)]
78. Fulignati, P. Clay Minerals in Hydrothermal Systems. *Minerals* **2020**, *10*, 919. [[CrossRef](#)]
79. Rosi, M.; Bertagnini, A.; Harris, A.J.L.; Pioli, L.; Pistolesi, M.; Ripepe, M. A case history of paroxysmal explosion at Stromboli: Timing and dynamics of the 5 April 2003 event. *Earth Planet. Sci. Lett.* **2006**, *243*, 594–606. [[CrossRef](#)]
80. Sieber, M.J.; Brink, F.J.; Leys, C.; King, P.L.; Henley, R.W. Prograde and retrograde metasomatic reactions in mineralised magnesium–silicate skarn in the Cu–Au Ertsberg East Skarn System, Ertsberg, Papua Province, Indonesia. *Ore Geol. Rev.* **2020**, *125*, 103697. [[CrossRef](#)]
81. Schreyer, W.; Maresch, W.V.; Daniels, P.; Wolfdorff, P. Potassic cordierite: Characteristic mineral for high–temperature, very low pressure environments. *Contrib. Mineral. Petrol.* **1990**, *105*, 162–172. [[CrossRef](#)]
82. Daniels, P.; Maresch, W.V.; Schreyer, W.; Sahl, K. Electron optical and X–ray powder diffraction study of synthetic and natural potassic cordierites. *Contr. Mineral. Petrol.* **1992**, *111*, 484–492. [[CrossRef](#)]
83. Vaughan, D.J.; Craig, J.R. Sulfide ore mineral stabilities, morphologies, and intergrowth textures. In *Geochemistry of Hydrothermal Ore Deposits*, 3rd ed.; Barnes, H.L., Ed.; Wiley–Interscience: New York, NY, USA, 1997; pp. 367–434.
84. Barton, P.B.; Skinner, B.J. Sulfide mineral stabilities. In *Geochemistry of Hydrothermal Ore Deposits*, 2nd ed.; Barnes, H.L., Ed.; Wiley–Interscience: New York, NY, USA, 1997; pp. 278–403.
85. Landi, P.; Métrich, N.; Bertagnini, A.; Rosi, M. Dynamics of magma mixing and degassing recorded in plagioclase at Stromboli (Aeolian Archipelago, Italy). *Contrib. Mineral. Petrol.* **2004**, *147*, 213–227. [[CrossRef](#)]
86. Witham, F.; Blundy, J.; Kohn, S.C.; Lesne, P.; Dixon, J.; Churakov, S.V.; Botcharnikov, R. SolEx: A model for mixed COHSCl–volatile solubilities and exsolved gas compositions in basalt. *Comput. Geosci.* **2012**, *45*, 87–97. [[CrossRef](#)]
87. Palm, A.B.; King, P.L.; Renggli, C.J.; Hervig, R.L.; Dalby, K.N.; Herring, A.; Mernagh, T.P.; Eggins, S.M.; Troitzsch, U.; Beeching, L.; et al. Unravelling the consequences of SO₂–basalt reactions for geochemical fractionation and mineral formation. *Rev. Mineral. Geochem.* **2018**, *84*, 257–283. [[CrossRef](#)]
88. Allard, P.; Aiuppa, A.; Loyer, H.; Carrot, F.; Gaudry, A.; Pinte, G.; Michel, A.; Dongarrà, G. Acid gas and metal emission rates during long-lived basalt degassing at Stromboli volcano. *Geophys. Res. Lett.* **2000**, *27*, 1207–1210. [[CrossRef](#)]
89. Lanzafame, G.; Ferlito, C.; Donato, S. Combining chemical and X–Ray microtomography investigations on crustal xenoliths at Mount Etna: Evidence of volcanic gas fluxing. *Ann. Geophys.* **2018**, *61*, 30. [[CrossRef](#)]
90. Calvari, S.; Spampinato, L.; Lodato, L.; Harris, A.J.L.; Patrick, M.R.; Dehn, J.; Burton, M.R.; Andronico, D. Chronology and complex volcanic processes during the 2002–2003 flank eruption at Stromboli volcano (Italy) reconstructed from direct observations and surveys with a handheld thermal camera. *J. Geophys. Res. Sol. Earth* **2005**, *110*, 1–23. [[CrossRef](#)]
91. Ripepe, M.; Marchetti, E.; Ulivieri, G.; Harris, A.; Dehn, J.; Burton, M.; Caltabiano, T.; Salerno, G. Effusive to explosive transition during the 2003 eruption of Stromboli volcano. *Geology* **2005**, *33*, 341–344. [[CrossRef](#)]
92. Pioli, L.; Rosi, M.; Calvari, S.; Spampinato, L.; Renzulli, A.; Di Robertom, A. The eruptive activity of 28 and 29 December 2002. In *The Stromboli Volcano: An Integrated Study of the 2002–2003 Eruption, Volume 182*; Calvari, S., Inguaggiato, S., Puglisi, G., Ripepe, M., Rosi, M., Eds.; American Geophysical Union: Washington, DC, USA, 2008; pp. 105–115.

-
93. Dempster, T.J.; Preston, R.J.; Bell, B.R. The origin of Proterozoic massif-type anorthosites: Evidence from interactions between crustal xenoliths and basaltic magma. *J. Geol. Soc.* **1999**, *156*, 41–46. [[CrossRef](#)]
 94. Preston, R.J.; Dempster, T.J.; Bell, B.R.; Rogers, G. The petrology of mullite-bearing peraluminous xenoliths: Implications for contamination processes in basaltic magmas. *J. Petrol.* **1999**, *40*, 549–573. [[CrossRef](#)]
 95. Bowen, N.L. The behaviour of inclusions in igneous magmas. *J. Geol.* **1922**, *30*, 513–570. [[CrossRef](#)]
 96. Nash, W.M.; Smythe, D.J.; Wood, B.J. Compositional and temperature effects on sulfur speciation and solubility in silicate melts. *Earth Planet. Sci. Lett.* **2019**, *507*, 187–198. [[CrossRef](#)]
 97. La Spina, G.; Burton, M.; de Michieli Vitturi, M. Temperature evolution during magma ascent in basaltic effusive eruptions: A numerical application to Stromboli volcano. *Earth Planet. Sci. Lett.* **2015**, *426*, 89–100. [[CrossRef](#)]